Towards a rational approach for multi-axial experimental campaigns for rubberlike material

Benjamin Martin, Erwan Verron, Michel Coret, Nathan Selles

Towards a rational approach for multi-axial experimental campaigns for rubberlike material

Benjamin Martin[a,b,*], Erwan Verron[a], Michel Coret[a], Nathan Selles[b]

[a]*Nantes Université, École Centrale de Nantes, CNRS, GeM, UMR6183, 1 rue de la Noe, Nantes, F-44000, , France*

[b]*Elanova, 60 rue Auber, Vitry-sur-Seine, F-94408, , France*

Abstract

This work takes up the developments around the logarithmic strain tensor and uses the invariants of this tensor to propose a new approach to multi-axiality of fatigue experiments for elastomers. This study leads to the introduction of a new notion, modality, which is intended as the microscopic counterpart of uni- and multi-axiality. This notion is quantified by the K_3 invariant (mode of deformation) of the logarithmic strain tensor, and is used to rationalize tension-torsion experimental campaigns. It is illustrated using two examples: the perfect cylinder and the AE2 "diabolo" sample. We then propose a methodology for building a test campaign based on this new definition.

Keywords:

Multi-axiality, Elastomers, Tension-torsion, Experimental campaign

*Corresponding author.
Benjamin Martin: benjamin.martin@ec-nantes.fr

1. Introduction

Soft materials such as elastomers, gels, and biological tissues have the ability to deform significantly without breaking. This ability is exploited in many industries, such as transport or energy for various applications, but also in the medical field. However, these properties go hand in hand with a complex mechanical response that must be carefully modeled in part design tools. In this context, uni-axial tensile tests are widely used to determine relevant constitutive equations of these materials (Case et al., 2015, Wang and Chester, 2018, Lane et al., 2018, Kim et al., 2023) as well as their fatigue properties (Hainsworth, 2007, Flamm et al., 2011, Shangguan et al., 2014).

Nevertheless, uni-axial tensile tests are rarely sufficient to completely characterize the three-dimensional mechanical response of soft materials. Indeed, in the case of complex loading of a part whose geometry is itself complex, it becomes necessary to account for the multi-axiality of strain and stress. With this in mind, two types of mechanical experimental campaigns can be distinguished to characterize the multi-axial response. Following the seminal work of Treloar (Treloar, 1944), the most common one simultaneously considers uni-axial tensile, biaxial tensile, and planar tension tests (see for example(Bitoh et al., 2011, Ahmad and Ajaj, 2022)). The second one is less classical and is motivated by the recent development of commercial characterization machines: it involves simultaneous tension along an axis and torsion around that axis (Suphadon and Busfield, 2009, Ayoub et al., 2011). The advantage of experiments is the experimental simplicity using only one

machine and one kind of sample. In the former type of experiments, the fitting of the parameters of the constitutive equation is made thanks to the analytical solutions of the simple loading tests (uni-axial tension, biaxial tension, and planar tension). In the latter type, the characterization is made using the analytical solution of tension-torsion test of the perfect cylinder (Suphadon and Busfield, 2009, Lectez et al., 2014).

Concerning fatigue, the multi-axial properties are mainly investigated using uni-axial tension and torsion tests, both can be combined to produce tension-torsion tests (Saintier et al., 2006a, Ayoub et al., 2011, 2012, Luo, 2020, Le Mire et al., 2021). These tension-torsion loading conditions are now the standard technique for the study of multi-axial fatigue in elastomers: a single and easy-to-produce specimen is used to investigate several deformation modes. This is reflected in the recent development of adapted commercial hydraulic or electric tension-torsion machines. While the tension-torsion test has been gradually standardized, the geometry of the corresponding samples differs from one study to another. However, as emphasized by Tee *et al.* all specimens belong to the same family referred to as diabolo, hourglass shape, or 3D dumbbell in bibliography (Tee et al., 2018). Such samples are designed to ensure that stress and strain concentrate in the center of the specimen, and that fatigue failure occurs in this zone. Example of such samples are shown in Fig. 1.

Even if all these diabolo samples (the term "diabolo" will be used through the rest of the paper) allow to explore the multi-axial response of soft mate-

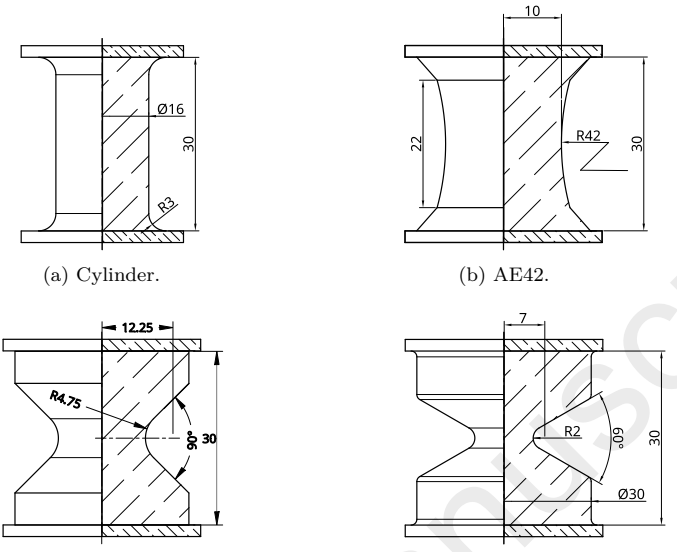

(a) Cylinder. (b) AE42.

(c) AN5. (d) AE2.

Figure 1: Examples of diabolo samples for tension-torsion experiments.

rials, the question of generalization arises: is it possible to compare results obtained with different experimental triplet sample/loading/material? For example, it is obvious that the perfect cylinder sample (Fig. 1a) and the AE2 sample (Fig. 1d) do not admit the same strain and stress distributions for similar loading conditions. The difficulties in comparing the response of these two samples are two-fold: the multi-axial nature of the fields and their inhomogeneity throughout the AE2 sample. So, it is difficult to compare two different experiments. At present, this question is avoided by defining tests in terms of the loading conditions prescribed by the machine. More specifically, this implies that the specimens can be in states of multi-axial deformation ranging from pure uni-axial tension to shear, since the machine

can impose all types of loading conditions between uni-axial tension and pure torsion (Harbour et al., 2008). A second question arises, how to define and quantify the multi-axiality of such an experimental triplet?

In the present work, we propose to revisit the definition of multi-axiality by adopting the "material viewpoint" rather than the machine one, i.e. local rather than global multi-axial strain and stress states. To avoid confusion, we use the term "modality" to refer to the local mode of deformation. Thanks to this new definition and digital tools, we propose a rational method to develop a multi-axial experimental campaign for fatigue of soft materials. Note that all tools used in the following are freely available to the reader (Martin et al., 2024).

The paper is organized as follow. The next section deals with the mechanics of the tension-torsion test of both perfect cylinder (Fig. 1a) and AE2 sample (Fig. 1d). Only these two sample geometries are considered because it is admitted that the mechanical response of other diabolo samples (Figs. 1b and 1c) follow the same trends. In Section 3, a thorough analysis of the strain field in AE2 specimens (made of materials with various stress-strain responses) allows us to propose a new local definition of uni- and multi-modality, and a method to develop a "multi-modal experimental campaign" for soft materials. Then a discussion on the influence of the material response on the stress in samples and on the previous definitions is proposed. Finally, the paper closes with a methodology to develop a multi-modal campaign for soft materials.

2. Mechanics of tension-torsion experiments

In this section, we first derive the deformation of both perfect cylinder and AE2 samples made of hyperelastic materials subjected to tension-torsion loading conditions. Then the strain fields are analyzed to propose a definition of their multi-axiality. In what follows, it is assumed that the loading conditions are prescribed displacements. This reflects the experimental techniques most often used for flexible materials, which differ from those for rigid materials (steel, composites, etc.), where the emphasis is on imposed forces.

2.1. The tension-torsion problem

2.1.1. Samples and loading conditions

As stated in the Introduction, two classical geometries of samples are considered: the perfect cylinder and the AE2 sample. The corresponding dimensions are presented in Fig. 2: the radius and the length of the perfect cylinder are respectively $A = 15$ mm and $L = 30$ mm, and the AE2 sample can be considered as a notched version of the perfect cylinder (the radius of curvature of the notch is equal to 2 mm); the AE2 sample is superimposed to the perfect cylinder in Fig. 2. Considering that these samples are deformed in a loading machine, the loading conditions are the vertical displacement U and the absolute angle α prescribed to the upper face of the sample, the lower face has been kept fixed.

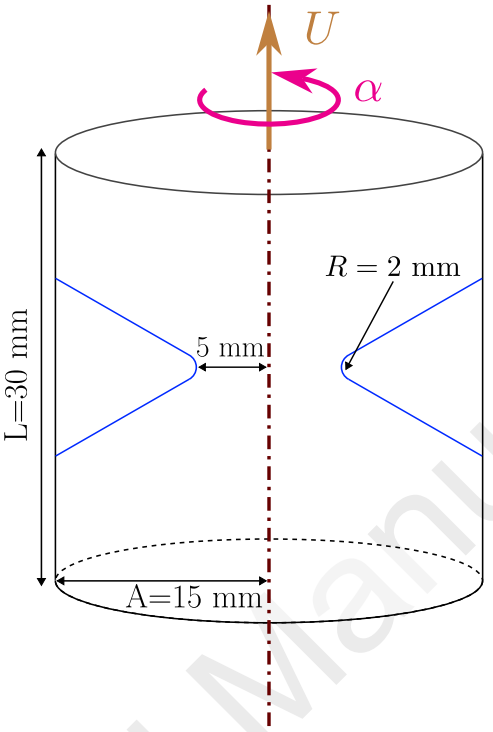

Figure 2: Perfect cylinder and AE2 samples: dimensions and loading conditions.

2.1.2. Constitutive equation

In a classical manner, rubber-like materials are considered homogeneous, isotropic and incompressible. Their elastic mechanical response is modeled by hyperelastic constitutive equations, based on the definition of an isotropic strain energy function W that depends on the two first invariants of the Cauchy-Green strain tensors (see for example (Boyce and Arruda, 2000, Marckmann and Verron, 2006)). Let first recall some basic notations in large strain continuum mechanics (Holzapfel, 2002). We consider the deformation of a body from a given reference configuration ($\mathcal{C}_0$) where the position of ma-

terial points is $\overrightarrow{X}$ to the current deformed configuration ($\mathcal{C}$) at time t defined by the position field $\overrightarrow{x}\left(\overrightarrow{X};t\right)$. The corresponding deformation gradient is

$$\boldsymbol{F} = \left.\frac{\partial \overrightarrow{x}}{\partial \overrightarrow{X}}\right|_t, \tag{1}$$

and the left Cauchy-Green strain tensor is defined as

$$\boldsymbol{b} = \boldsymbol{F}\,\boldsymbol{F}^T, \tag{2}$$

where the superscript $\cdot^T$ stands for the transposition. The two first principal invariants of $\boldsymbol{b}$ are

$$I_1 = \mathrm{tr}(\boldsymbol{b}) \tag{3}$$

and

$$I_2 = \frac{1}{2}\left[I_1^2 - \mathrm{tr}(\boldsymbol{b}^2)\right], \tag{4}$$

in which $\mathrm{tr}(\cdot)$ is the trace. Note that the third principal invariant, $\det \boldsymbol{b}$ ($\det(\cdot)$ being the determinant), is always equal to 1, due to the incompressible nature of the considered materials.

Here, in order to investigate the influence of the stress-strain response of the material on the results, nine possible material responses are considered. They are all based on the Arruda-Boyce (or 8-chains) definition of the strain

energy function (Arruda and Boyce, 1993):

$$W_{\mathrm{AB}}\left(I_1\right) = \mu {\lambda_m}^2 \left[\sqrt{\frac{I_1}{3\lambda_m^2}}\eta + \log\left(\frac{\eta}{\sinh\eta}\right)\right] \tag{5}$$

with

$$\eta = \mathcal{L}^{-1}\left(\sqrt{\frac{I_1}{3\lambda_m^2}}\right). \tag{6}$$

In this equation $\mathcal{L}(\cdot)$ stands for the Langevin function, and (μ, λ_m) are the two material parameters: the former is the shear modulus and the latter is the maximum stretch a polymer chain can undergo (it is related to the chain length). So the nine material response are defined by the combinations of the following values of the parameters: $\mu = \{0.1,\ 1.0,\ 10.0\}$ MPa and $\lambda_m = \{1,\ 3,\ 200\}$. The values for the shear modulus μ are respectively representative of unfilled silicon rubber (Gour and Kumar, 2022), polymers such as PDMS (Nunes, 2010) and filled charged rubber (Yang et al., 2007). The values for the maximum chain extension λ_m are also representative of the different stretch ratios required to reach the hardening of the strain-stress curve (Gour and Kumar, 2022). Note that the three models defined with $\lambda_m = 200$ reduce to the classical neo-Hookean formulation for realistic strain levels because the stretch ratio necessary to activate the strain-hardening is about 1,000% which will not be considered in the present study.

Similarly than in Arruda and Boyce (1993), the finite element Abaqus software used in the present study considers an approximate form of the model based on the five-term series expansion of the inverse Langevin func-

tion:

$$W\left(I_1\right) \approx \mu \sum_{i=1}^{5} \frac{C_i}{{\lambda_m}^{2i-2}} \left(I_1^i - 3^i\right), \tag{7}$$

where $C_1 = 1/2$, $C_2 = 1/20$, $C_3 = 11/1050$, $C_4 = 19/7000$, and $C_5 = 519/673750$ MPa. It is possible to calculate the effective (or initial) shear modulus μ_0:

$$\mu_0 = \mu \left(1 + \frac{3}{5\lambda_m^2} + \frac{99}{175\lambda_m^4} + \frac{513}{875\lambda_m^6} + \frac{42039}{67375\lambda_m^8}\right). \tag{8}$$

The corresponding values are given in Table 1.

		λ_m		
		1	3	200
μ [MPa]	0.1	0.338	0.107	0.1
	1.0	3.38	1.07	1.0
	10.0	33.8	10.7	10.0

Table 1: Initial shear modulus μ_0 [MPa] of the nine material responses.

For a given deformation described by the left Cauchy-Green tensor $\boldsymbol{b}$, the true stress tensor $\boldsymbol{\sigma}$ is (where q is a Lagrange multiplier related to the incompressibility and $\boldsymbol{I}$ is the identity tensor):

$$\boldsymbol{\sigma} = -q\boldsymbol{I} + 2\frac{\partial W}{\partial I_1}\boldsymbol{b}. \tag{9}$$

The nominal (first Piola-Kirchhoff) and true (Cauchy) stress of the uni-

axial compression-tension response of the model are:

$$P = 2\frac{\partial W}{\partial I_1}\left(\lambda - \frac{1}{\lambda^2}\right) \approx 2\mu \sum_{i=1}^{5} i \frac{C_i}{{\lambda_m}^{2i-2}} {I_1}^{i-1}\left(\lambda - \frac{1}{\lambda^2}\right), \tag{10}$$

and

$$\sigma = 2\frac{\partial W}{\partial I_1}\left(\lambda^2 - \frac{1}{\lambda}\right) \approx 2\mu \sum_{i=1}^{5} i \frac{C_i}{{\lambda_m}^{2i-2}} {I_1}^{i-1}\left(\lambda^2 - \frac{1}{\lambda}\right), \tag{11}$$

respectively. λ is the stretch ratio in the loading direction ($\lambda > 1$ for tension, $\lambda < 1$ for compression). The corresponding stress-stretch curves for the nine sets of parameters of Tab. 1 are shown in Fig. 3. As emphasized above,

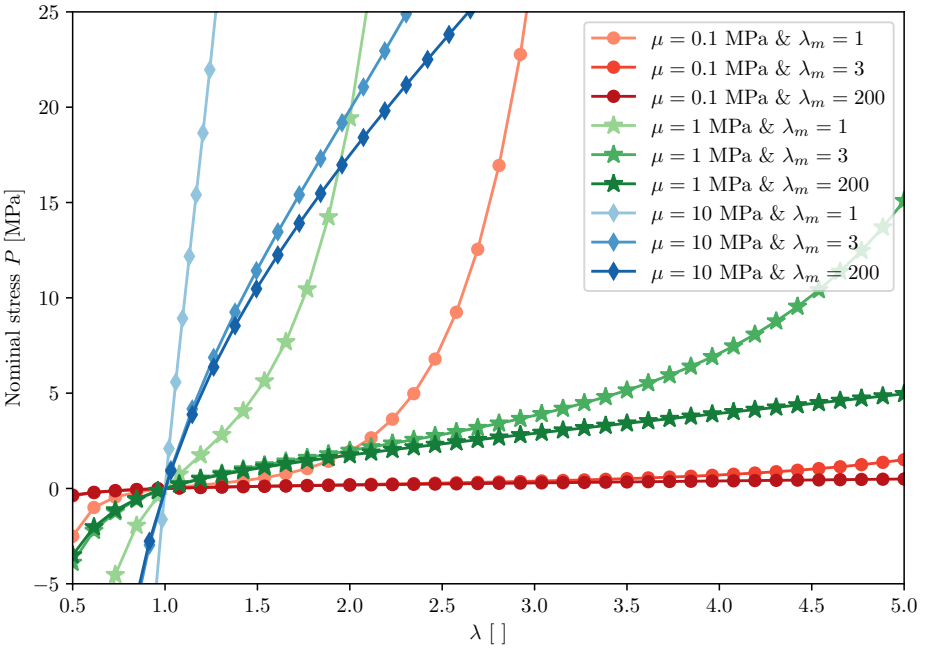

Figure 3: uni-axial tension-compression stress-strain response of the nine models (nominal stress vs. stretch ratio).

depending on the values of the material parameters, very different mechanical responses are obtained in the considered strain range ($0.5 \leq \lambda \leq 5.0$). As example, for ($\mu = 0.1$ MPa, $\lambda_m = 1$) the curve corresponds to a very soft material with strain-hardening, e.g. a hydrogel, for ($\mu = 10$ MPa, $\lambda_m = 3$) it corresponds to a rigid polymer (convex curve), and for ($\mu = 1$ MPa, $\lambda_m = 3$) we recover the classical S-shaped curve of elastomers.

2.1.3. Kinematics of the samples under tension-torsion loading

Analytical model of the perfect cylinder. The governing equations of the simultaneous tension and torsion of a perfect cylinder are well-known (see for example (Rivlin and Rideal, 1949, Ciarletta and Destrade, 2014)); they are briefly recalled in the following. The problem and the necessary notations are defined in Fig. 4. The cylinder of nominal radius A and length L deforms into a cylinder of radius a and length l. Consider a material point $P_0(R, \Theta, Z)$ in the reference configuration ($\mathcal{C}_0$) that transforms into $P(r, \theta, z)$ in the deformed configuration $()\mathcal{C}$). We denote $(\vec{e_R}, \vec{e_\Theta}, \vec{e_Z})$ the coordinate system in the reference configuration and $(\vec{e_r}, \vec{e_\theta}, \vec{e_z})$ the coordinate system in the deformed configuration. Thus, the corresponding positions in ($\mathcal{C}_0$) and ($\mathcal{C}$) are

$$\overrightarrow{X}(P_0) = R\vec{e_R} + Z\vec{e_Z} \quad \text{and} \quad \overrightarrow{x}(P) = r\vec{e_r} + z\vec{e_z}. \tag{12}$$

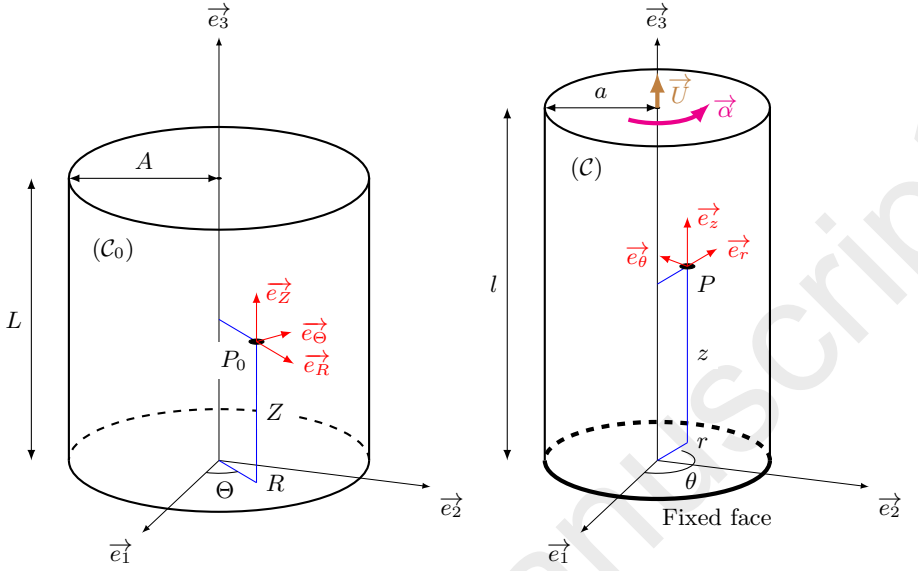

Figure 4: Deformation of a perfect cylinder under tension-torsion loading conditions.

The kinematical equations that transform these positions are

$$\begin{cases} r = \dfrac{1}{\sqrt{\lambda}} R, \\ \theta = \Theta + \tau \lambda Z, \\ z = \lambda Z, \end{cases} \tag{13}$$

where λ is the macroscopic stretch ratio in the $\vec{e_Z}$ direction and τ is the torsion angle per unit of deformed length. They are related to the vertical

displacement U and the prescribed rotation α by

$$\begin{cases} \lambda = \dfrac{l}{L} = 1 + \dfrac{U}{L}, \\ \tau = \dfrac{\alpha}{l} = \dfrac{\alpha}{\lambda L}. \end{cases} \tag{14}$$

The corresponding deformation gradient tensor is given by

$$\boldsymbol{F} = \frac{1}{\sqrt{\lambda}}\left(\vec{e_r} \otimes \vec{e_R} + \vec{e_\theta} \otimes \vec{e_\Theta}\right) + R\tau\sqrt{\lambda}\vec{e_\theta} \otimes \vec{e_Z} + \lambda\vec{e_z} \otimes \vec{e_Z}, \tag{15}$$

and the principal stretch ratios can be easily calculated; they reduce to

$$\lambda_I = \sqrt{\frac{\beta + \sqrt{\beta^2 - 4\lambda}}{2}}, \tag{16}$$

$$\lambda_{II} = \frac{1}{\sqrt{\lambda}}, \tag{17}$$

$$\lambda_{III} = \sqrt{\frac{\beta - \sqrt{\beta^2 - 4\lambda}}{2}}, \tag{18}$$

with

$$\beta = R^2\tau^2\lambda + \lambda^2 + \frac{1}{\lambda}. \tag{19}$$

Numerical model of the AE2 sample. In contrast to the previous case, the tension-torsion of the AE2 sample does not admit analytical solution and the problem must be solved numerically. As mentioned above, the commercial Abaqus finite element software is used and the previous constitutive models is considered. The numerical model is axisymmetric with possible

out-of-plane twisting. The vertical section of the sample is meshed with 3,876 CGAX8H (8-node biquadratic, axisymmetric stress/displacement hybrid with linear pressure and twist) finite elements, as shown in Fig. 5a. The

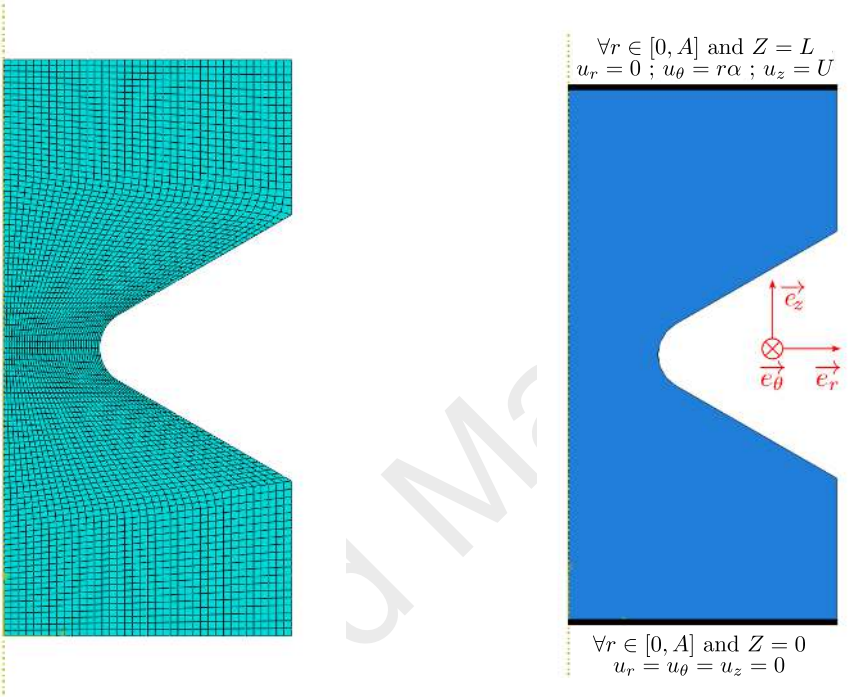

(a) Mesh of the AE2 sample.

(b) Loading conditions.

Figure 5: Axisymmetric numerical model of the AE2 sample.

loading conditions consist in a vertical displacement U and a torsion angle α prescribed on the upper face and zero displacement of the lower face of the sample is fixed throughout the simulation, as shown in Fig. 5b.

2.2. Definition of multi-axiality for tension-torsion of the samples

2.2.1. The invariants of the Hencky strain tensor

A milestone in the quantification of multi-axiality for deformed soft materials was reached by Criscione *et al.* (Criscione et al., 2000). In their paper, the authors derive three particular invariants of the Hencky (or logarithmic or true) strain tensor, denoted $\boldsymbol{h}$ in the following, to describe a given state of deformation. This proposal can be seen as the kinematic counterpart of the classical Lode invariants (or coordinates) of the Cauchy stress tensor widely used in metal plasticity (see for example Brannon (2007)).

The Hencky strain tensor, also referred to as true or logarithmic strain tensor, is defined as

$$\boldsymbol{h} = \frac{1}{2}\log(\boldsymbol{b}). \tag{20}$$

Criscione *et al.* derive the three following invariants:

- the change in volume

$$K_1 = \mathrm{tr}\,(\boldsymbol{h}) = \log(J), \tag{21}$$

  where $J = \det \boldsymbol{F}$ is the Jacobian of the deformation,

- the magnitude-of-distorsion

$$K_2 = \sqrt{\mathrm{dev}\,(\boldsymbol{h}) : \mathrm{dev}\,(\boldsymbol{h})}, \tag{22}$$

  in which $\mathrm{dev}\,(\cdot)$ stands for the deviatoric part of a tensor: $\mathrm{dev}\,(\cdot) =$

$\cdot - \boldsymbol{I}\mathrm{tr}\,(\cdot)\,/3,$

- the mode-of-distorsion

$$K_3 = \frac{3\sqrt{6}}{K_2^3}\det\left[\mathrm{dev}\,(\boldsymbol{h})\right] \tag{23}$$

which takes values between -1 and 1: $K_3 = -1$ for uni-axial compression and equibiaxial tension, $K_3 = 0$ for simple shear and planar tension, and $K_3 = 1$ for uni-axial tension and equibiaxial compression.

In the special case of incompressible materials, $J = 0$ then $K_1 = 0$, and $\mathrm{dev}\,(\boldsymbol{h}) = \boldsymbol{h}$. Moreover, considering the three principal stretch ratios $(\lambda_i)_{i=I,II,III}$, the two non-null invariants can be written as

$$K_2 = \sqrt{\log\left(\lambda_I\right)^2 + \log\left(\lambda_{II}\right)^2 + \log\left(\lambda_{III}\right)^2}, \tag{24}$$

and

$$K_3 = \frac{3\sqrt{6}}{{K_2}^3}\log\left(\lambda_I\right)\log\left(\lambda_{II}\right)\log\left(\lambda_{III}\right). \tag{25}$$

It is to note that these invariants represent a local measure of the deformation state: they are defined in each point of the body.

Remark on the physical meaning of the invariants. The two considered invariants are not usual in the study of the elastomers subjected to large strain. The magnitude-of-distorsion K_2, defined by Eq. (24), is the logarithmic counterpart of the principal Cauchy-Green strain invariant I_1 (Eq. (3)), which is

the basic kinematic quantity for hyperleastic models, whether phenomenological (Yeoh or Mooney-Rivlin models for example) or derived from the statistical rubber elasticity theory (neo-Hookean or 8-chains models for example). The mode-of-distorsion K_3, defined by Eq. (25) describes the way the material is deformed and it echoes the importance of the various experiments (uni-axial, planar and equibiaxial tension) in model fitting (Treloar, 1944, Kawabata et al., 1981).

2.2.2. Application to the perfect cylinder sample

Using Eqs (24-25) and (16-19) and after some basic algebraic manipulations, it is possible to calculate the functions $K_2(\lambda, \tau)$ and $K_3(\lambda, \tau)$ at any points of the cylinder throughout the deformation. For a given radius, these two functions do depend on neither the vertical position z or the initial angle Θ.

Let consider a material point on the external surface of the cylinder, i.e. $R = A$. For numerous loading conditions $U \in [-2, 10]$ mm and $\alpha \in [0, 100]°$, it is possible to compute and plot the "maps" of the invariants K_2 and K_3 with respect to the loading parameters λ and τ. The corresponding results are shown in Fig. 6. The K_2-map (Fig. 6a) shows the magnitude-of-distortion in points of the external surface with respect to the loading conditions (λ, τ) applied to the sample. The solid black curves represent the contour lines of K_2. The K_3-map (Fig. 6b) presents the mode-of-distortion as a function of the loading conditions (λ, τ). The two dotted black lines highlights special

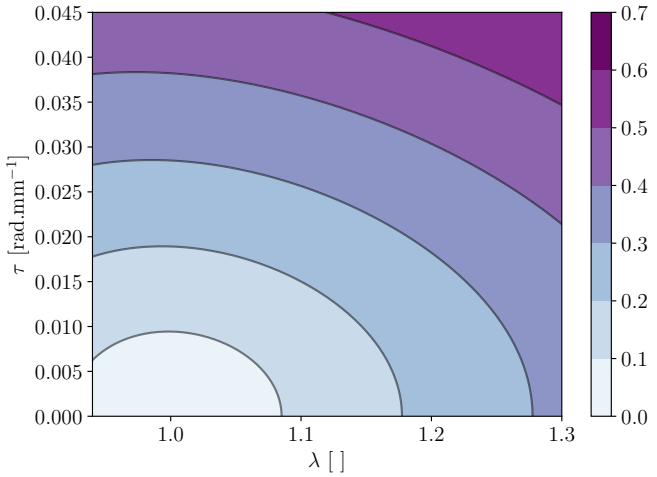

(a) K_2.

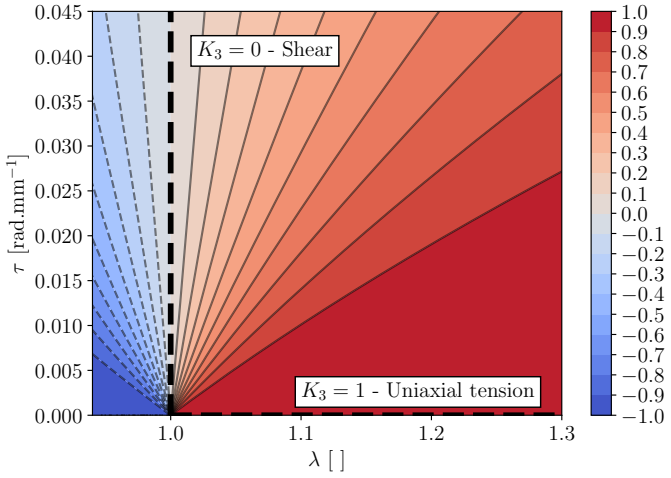

(b) K_3.

Figure 6: Maps of the invariants of the Hencky strain tensor for the perfect cylinder.

values of K_3: the horizontal line $\tau = 0$ corresponds to $K_3 = 1$ which is generally associated with uni-axial tension and the vertical line $\lambda = 1$ corresponds

to $K_3 = 0$ associated with simple shear which is obtained by pure torsion. It is to note that the iso-K_3 curves are not evenly distributed in the (λ, τ)-plane: as example a large part of the plane corresponds to $K_3 \in [0.9, 1]$, i.e. near uni-axial tension conditions. It should be noted that applying a (λ,τ) loading, and therefore the corresponding machine prescriptions (U,α), to keep K_2 or K_3 constant throughout an experiment, we need to interpolate the contour lines of either card.

2.2.3. Application to the AE2 sample

Conversely to the perfect cylinder sample, the kinematics of the AE2 sample subjected to tension-torsion is not known. Moreover, the kinematic fields are not homogeneous as shown in Fig. 7. Thus, the maps of the invariants

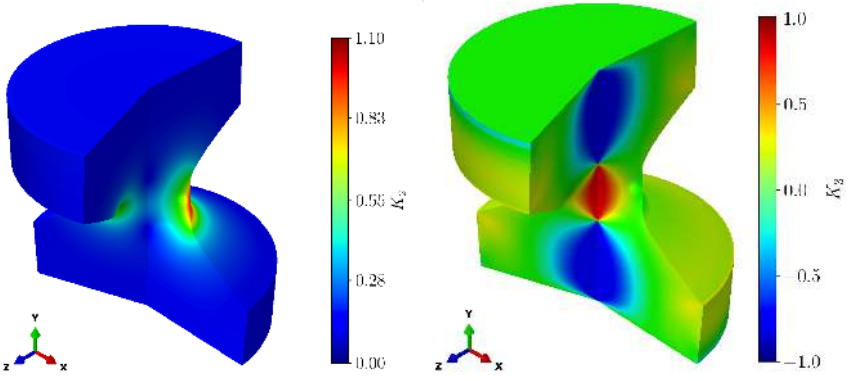

(a) K_2. (b) K_3.

Figure 7: Isovalues of Hencky's tensor invariants in AE2 samples.

are more difficult to compute: they necessitate to solve the complete mechanical problem for every possible couples (λ, τ). The results are collected

and post-treated as follow.

The numerical method developed to produce the counterpart of Fig. 6 for the AE2 sample is now presented.

1. The range of loading conditions is chosen. It consists of magnitude intervals and steps for the global displacement U and the torsion angle α which are denoted $(U^i)_{i=1..n}$ and $(\alpha^j)_{j=1..m}$ respectively. It leads to the corresponding ranges of λ and τ thanks to Eq. (14). Minimum, maximum and step values of the loading conditions are set by the user.
2. For each pair (U_i, α_j), the finite element computation is performed. To limit the number of computations, a series of fixed torsion angle α_j simulations is performed: for each j, a given simulation consists in prescribing an increasing top displacement from U_1 to U_n.
3. A UVARM subroutine is added in Abaqus to compute the invariants K_2 and K_3 from the Hencky strain tensor. Then, at each node of the mesh, the invariants K_2 and K_3 are computed for the considered loading conditions. Practically, a Python script executed by the Abaqus internal interpreter automates the simulations, projects the values of invariants at Gauss points onto the nodes, and then extracts data.
4. For the nodes (or material points) chosen, all corresponding values of the invariants are extracted. An interpolation function is applied to the data to produce the K_2- and K_3-maps for all these nodes. Practically, a second Python script is used to post-process the data extracted at the nodes chosen by the user and the multiquadratic radial-based

functions implemented in Python *Scipy.interpolate* module are used to interpolate the mapping (Scipy Community).

In the following, only one node is retained: the node on the external surface at the mid-section of the sample (the material point at which the fatigue cracks should initiate).

3. Results

In the following the previous numerical technique is used to investigate the influence of the material response on the maps of invariants for the AE2 sample. Then, thanks to these results and the perfect cylinder ones, definitions of uni- and multi-modality of experiments are proposed. Finally, the concept of "multi-modal experimental campaign" is proposed.

3.1. Maps of invariants for the AE2 sample

For each invariants, K_2 and K_3, the maps corresponding to the nine material models defined in Section 2.1.2 are drawn and commented.

3.1.1. Magnitude-of-distortion K_2

Fig. 8 presents the maps of K_2 for the AE2 sample; for the sake of clarity, the organization of the sub-figures is the same than in the Tab. 1. First, Fig. 8 shows that only the limiting stretch λ_m influences the map: for a column (same λ_m, different μ) the three maps are almost identical. On the contrary for a given row (different λ_m, same μ) the three maps differ. More precisely, for the same load, the value of K_2 increases with the value of λ_m.

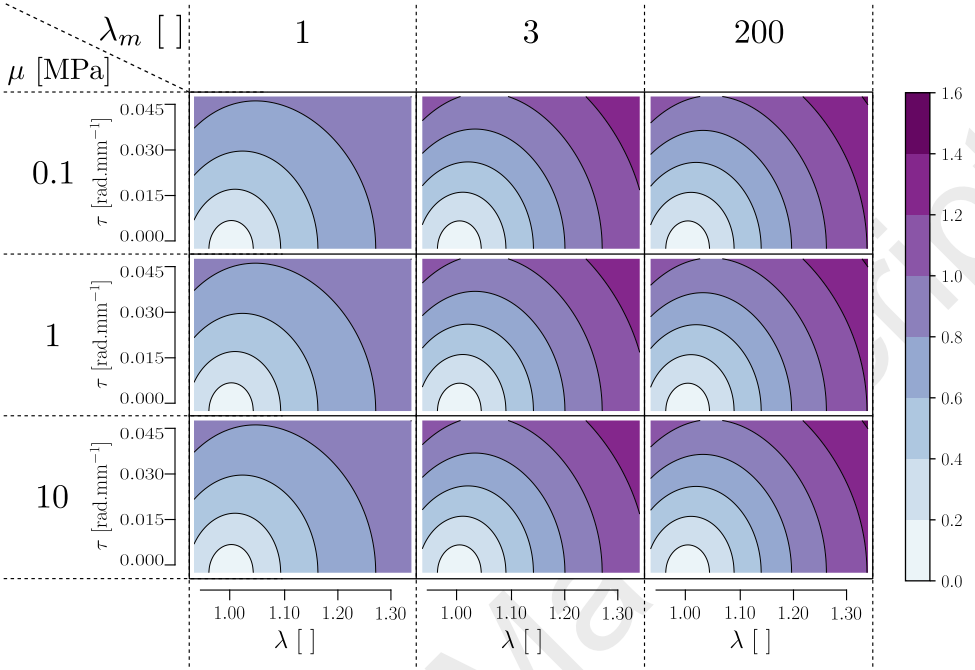

Figure 8: Maps of K_2 for the nine material models.

This evolution can be explained by the physical meanings of the invariant and the parameter. The invariant K_2 is the magnitude-of-distorsion, and the larger the strain the material undergoes, the larger the value of the invariant is. The parameter λ_m describes the length of the chains, and the higher its value, the longer the chains making up the polymer. Thus, low values of λ_m imply a lower maximum extension and therefore a lower value of K_2 than for high values of λ_m.

Second, for all plots in Fig. 8 the magnitude-of-distortion is higher in the AE2 sample than in the perfect cylinder (Fig. 6 left), for both tension ($\lambda > 1$) and compression ($\lambda < 1$). This result is easily explained by the effect

of strain and stress concentration in the AE2 sample due to the notch.

3.1.2. Mode-of-distorsion K_3

Fig. 9 presents the maps of K_3 for the AE2 sample; for the sake of clarity, the organization of the sub-figures is the same than in Tab. 1.

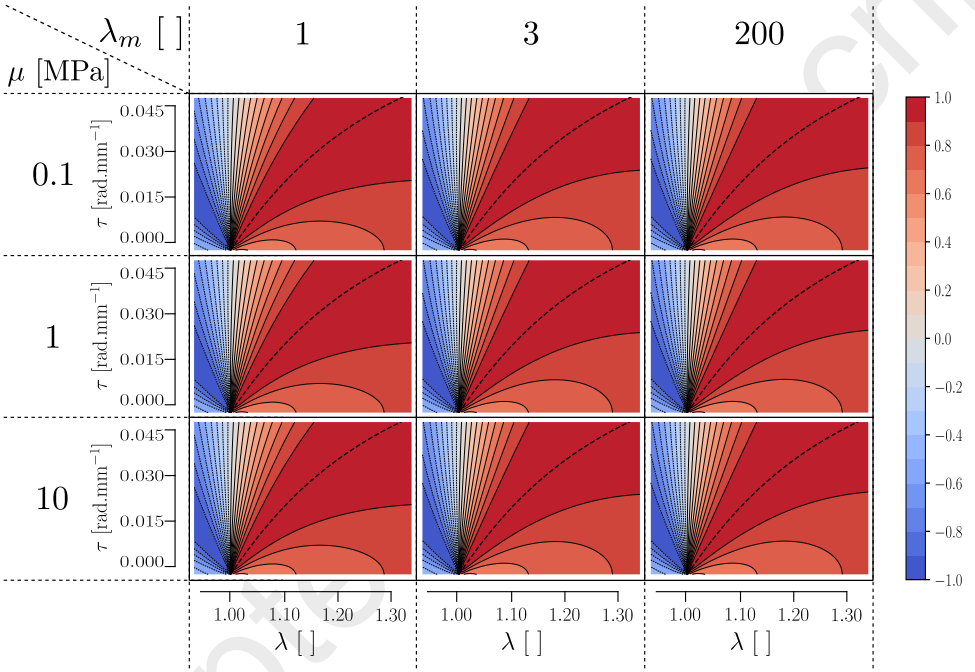

Figure 9: Maps of K_3 for the nine materials. The bold dotted black line correspond to constant mode-of-deformation $K_3 = 1$.

Similarly than for the magnitude, Fig. 9 shows that only λ_m influences the distribution in the maps (same maps in column, different ones in row). To highlight this influence, Fig. 10 presents the (λ, τ) paths that keep K_3 constant at the notch during a loading cycle, for the three materials defined by $\mu = 1$ MPa and $\lambda_m = 1$, 3, 200 (the three maps of the central column

in Fig. 9). Two deformation states are considered: $K_3 = 1$, in Fig. 10a and,

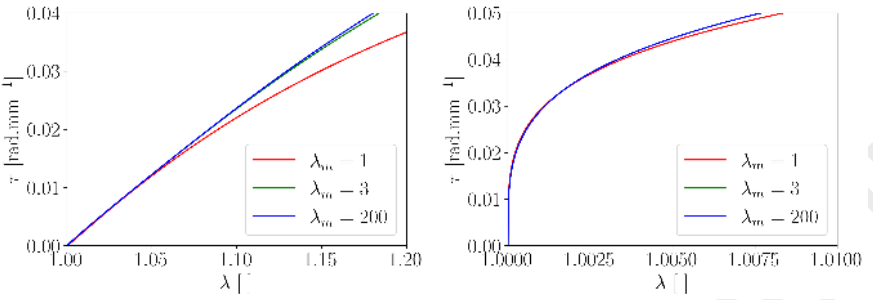

(a) Curves associated with $K_3 = 1$.

(b) Curves associated with $K_3 = 0$.

Figure 10: Loading paths to maintain K_3 constant at the notch throughout the experiment, for the three values of λ_m.

$K_3 = 0$ in 10b. As emphasized in Fig. 10a maintaining uni-axial tension $K_3 = 1$ at the notch of the sample necessitates to apply mixed tension-torsion loading conditions ($\tau \neq 0$). It highly differs from the perfect cylinder for which the deformation mode $K_3 = 1$ on the external surface is simply induced by uni-axial tensile loading conditions ($\tau = 0$). A similar observation applies for shear in Fig. 10a, even if in this case the difference with the perfect cylinder is small as shown by the values of λ involved (less than 1.02).

3.2. Definitions

Thanks to the previous results, it is now possible to propose several definitions.

3.2.1. Uni- vs. multi-modal experimental test

On the one hand, multi-axiality is defined theoretically by the state of strain (for soft materials) or stress (for rigid materials) in the gauge length

of the sample. On the other hand, it is experimentally linked to the loading conditions prescribed by the testing machine (tensile-torsion tests in Ayoub et al. (2011) or equibiaxial tensile test in Treloar (1944) for example). This difference in definition can lead to ambiguity in the interpretation of results, as the state of strain (or stress) is never homogeneous in a real sample. For example, during fatigue tests carried out by Le Mire (2022) on cylindrical specimens (Saintier et al., 2006b, Le Mire et al., 2021), fatigue cracks often appear at the foot of the specimen where the targeted state of strain for the gauge length is not respected.

To overcome this ambiguity, we propose "local" definitions, i.e. definitions that applies at a material point. To avoid any confusion with the classical terms of uni- and multi-axiality widely used in experimental studies, the term "modality" (in reference to "mode-of-distorsion" used in Criscione et al. (2000)) is introduced to qualify experimental tests in the light of their local strain states.

Definition 1. *An experimental test is "uni-modal at a given material point" if K_3 remains constant at this point throughout the test.*

Definition 2. *On the contrary, an experimental test is "multi-modal at a given material point" if K_3 varies during the test.*

Note that these definitions apply for both monotone experiments, for example to fit a constitutive equation, and cyclic experiments, for example for fatigue investigations. It should be added that while the second definition covers a very wide variety of tests, multi-modal iso-K_2 tests are interesting cases among them.

3.2.2. Multi-modal experimental campaign

Thanks to the two previous definitions and the mapping tools proposed above, it is now possible to propose different methods to develop a multi-axial experimental campaign. They can be represented in the K_3-map as exemplified in Fig. 11.

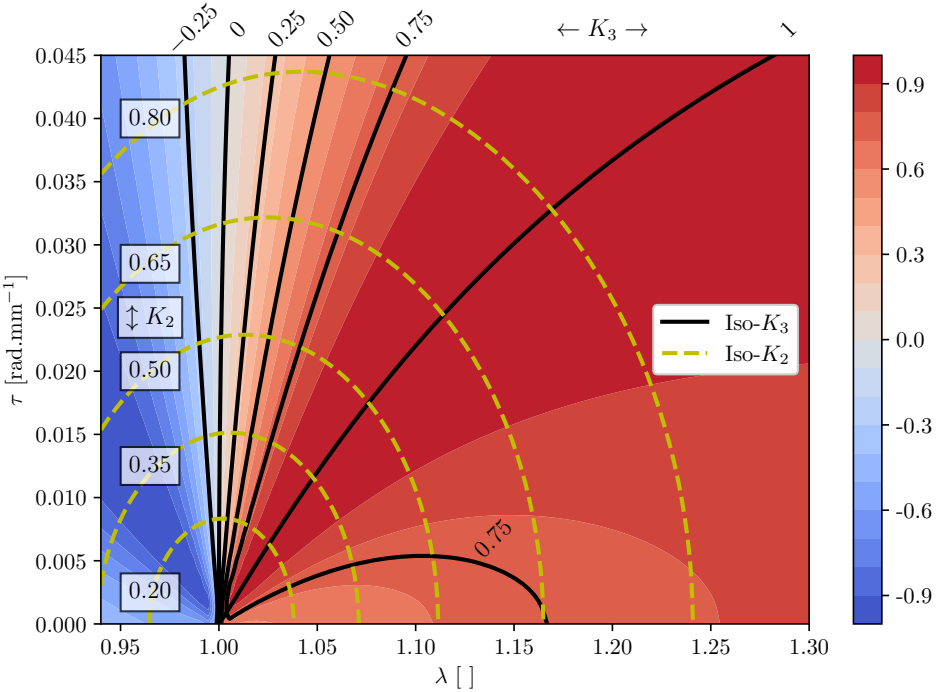

Figure 11: Two possible multi-axial campaigns: a series of uni-modal experimental tests in black (iso-K_3) and a series of multi-modal experimental tests in yellow dashed line (iso-K_2). The map corresponds to the material with $\mu = 0.1$ MPa and $\lambda_m = 1$.

To recover the notations of Fig. 2, the loading conditions (λ, τ) corresponding to these experiments can be easily converted into $U(t)$ and $\alpha(t)$ input signals that are applied by the testing machine (see Eq. (14)). The

corresponding machine loading paths for the uni-modal case $K_3 = 1$ and for the multi-modal case $K_2 = 0.5$ are shown in Fig. 12. For the AE2 geometry, the vertical displacement U and the torsion angle α can be out-of-phase to maintain constant the corresponding invariant. To keep the mode of deformation constant $K_3 = 1$, the torsion angle α has to be non zero and the angle has to be large: Fig. 12a shows that for a vertical displacement $U \approx 9$ mm, the torsion angle is approximately 100°.

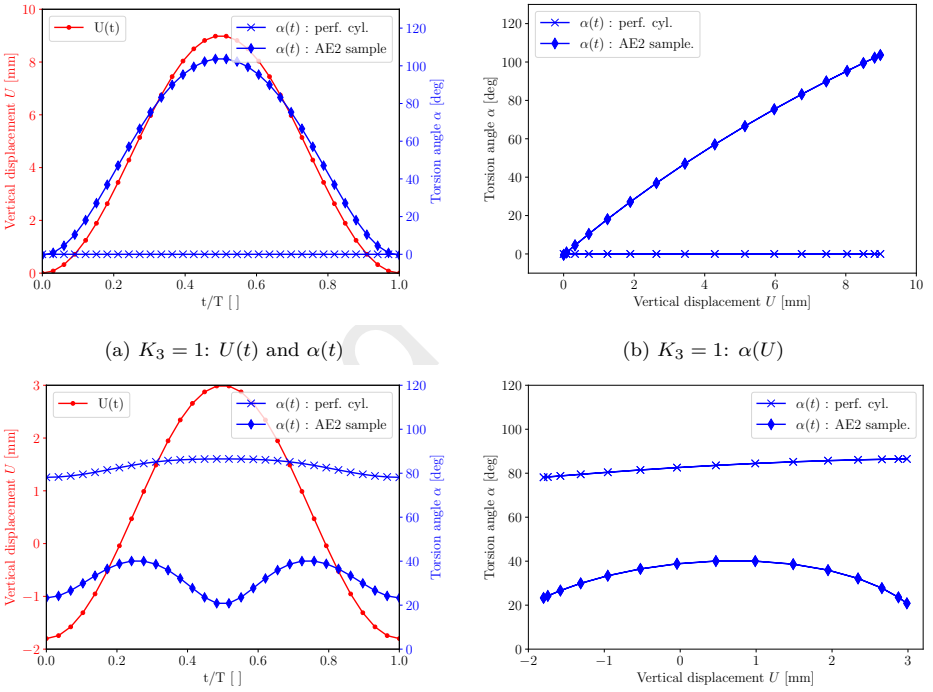

(a) $K_3 = 1$: $U(t)$ and $\alpha(t)$

(b) $K_3 = 1$: $\alpha(U)$

(c) $K_2 = 0.5$: $U(t)$ and $\alpha(t)$

(d) $K_2 = 0.5$: $\alpha(U)$

Figure 12: Vertical displacement and twist angle associated with $K_3 = 1$ and $K_2 = 0.5$ for AE2 sample and comparison with the perfect cylinder case.
The paths correspond to the material model with $\mu = 0.1$ MPa and $\lambda_m = 1$.

4. Discussion

The previous developments are entirely based on the kinematics of the tension-torsion problem. Such approach is consistent with machine control for testing of soft materials: displacements and angles are prescribed, and forces and torques are measured. Nevertheless, in the large majority of studies the mechanical loading modes are defined with respect to stress rather than strain; for example uni-axial tension corresponds to an uni-axial stress tensor.

In the following, we first discuss the stress tensor along the loading path for the uni-modal case $K_3 = 1$, then along the loading path for the uni-modal case $K_3 = 0$. Without loss of generality, the next investigations focus on the first material model of the series, defined by $\mu = 0.1$ MPa and $\lambda_m = 1$. It corresponds to the maps of the upper left corner in Figs 8 and 9, the one in Fig. 11.

4.1. $K_3 = 1$: uni-axial tension

In order to apply the loading conditions that corresponds to the dotted black line of the upper left map in Fig. 9, the corresponding function $\tau(\lambda)$ is fitted by a simple power function

$$\tau(\lambda) = \sum_{i=1}^{3} a_i \left(\lambda - 1\right)^{\beta_i} . \tag{26}$$

The corresponding values of the parameters $(a_i, \beta_i)_{i=1,2,3}$ are given in Table 2.

a_1	β_1	a_2	β_2	a_3	β_3
-1.637	1.896	0.396	1.090	1.344	2.103

Table 2: Parameters of Eq. 26 for the function $\tau(\lambda)$ such that $K_3 = 1$.

Thanks to this interpolating function, it is now possible to simulate the path $K_3 = 1$ with Abaqus. The corresponding history of the Cauchy stress tensor at our point of interest at the notch is extracted and expressed in the basis $(\vec{e_R}, \vec{e_\Theta}, \vec{e_Z})$ of the undeformed configuration. Same is done for the Hencky's strain tensor. These tensors are diagonalized throughout the loading path and the principal stresses (respectively stretch ratios) are denoted σ_I, σ_{II} and σ_{III} (respectively λ_I, λ_{II} and λ_{III}). The convention used here is $\sigma_I \geq \sigma_{II} \geq \sigma_{III}$ (respectively $\lambda_I \geq \lambda_{II} \geq \lambda_{III}$). Moreover, the Baker and Ericksen inequality states that the principal stresses σ_i have the same ordering than the principal stretches ratios λ_i (Baker and Ericksen, 1954),

$$\frac{\sigma_i - \sigma_j}{\lambda_i - \lambda_j} > 0 \text{ with } i \neq j. \tag{27}$$

Here, the principal stretch ratios are derived from the diagonalization of Hencky's tensor.

In the classical case of uni-axial tension (UT), tensors $\boldsymbol{b}$ and $\boldsymbol{\sigma}$ can be

written, in the eigenvector basis $\mathcal{B}_p$:

$$\boldsymbol{b}^{UT} = \begin{bmatrix} {\lambda_I}^2 & & \\ & {\lambda_{II}}^2 & \\ & & {\lambda_{III}}^2 \end{bmatrix}_{\mathcal{B}_p} = \begin{bmatrix} {\lambda_I}^2 & & \\ & 1/\lambda_I & \\ & & 1/\lambda_I \end{bmatrix}_{\mathcal{B}_p} \tag{28}$$

and

$$\boldsymbol{\sigma}^{UT} = \begin{bmatrix} \sigma_I & & \\ & \sigma_{II} & \\ & & \sigma_{III} \end{bmatrix}_{\mathcal{B}_p} = \begin{bmatrix} \sigma^{UT} & & \\ & 0 & \\ & & 0 \end{bmatrix}_{\mathcal{B}_p}. \tag{29}$$

Using the Arruda-Boyce hyperelastic model (Eq. (7)), the analytical non-zero component of the Cauchy stress tensor is,

$$\sigma^{UT} = 2\frac{\partial W}{\partial I_1}\left({\lambda_I}^2 - \frac{1}{\lambda_I}\right) \approx 2\mu \sum_{i=1}^{5} i \frac{C_i}{{\lambda_m}^{2i-2}} {I_1}^{i-1} \left({\lambda_I}^2 - \frac{1}{\lambda_I}\right). \tag{30}$$

Fig. 13 compares the eigenvalues obtained numerically with Abaqus and the analytical values for both $\boldsymbol{b}$ and $\boldsymbol{\sigma}$. Plots are functions of the reduced time of the simulation t/T for the principal stretch ratios (Fig. 13a) and as functions of the largest principal stretch ratio λ_I for the principal true stresses (Fig. 13b). It confirms the state of uni-axial stress at the material point under consideration.

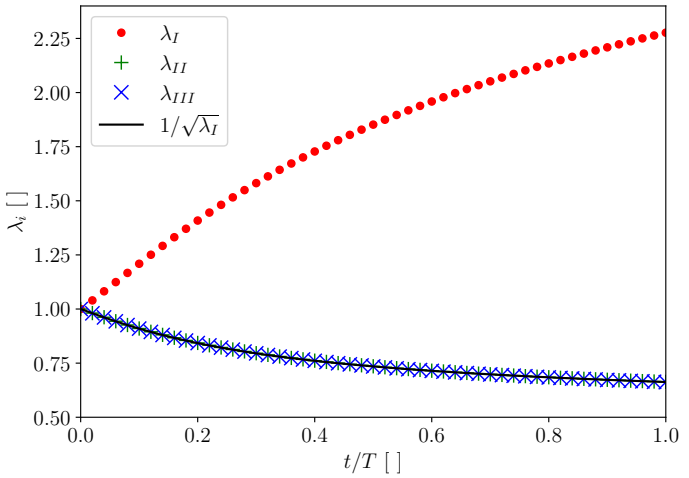

(a) Principal stretch ratios λ_i as function of reduced time t/T.

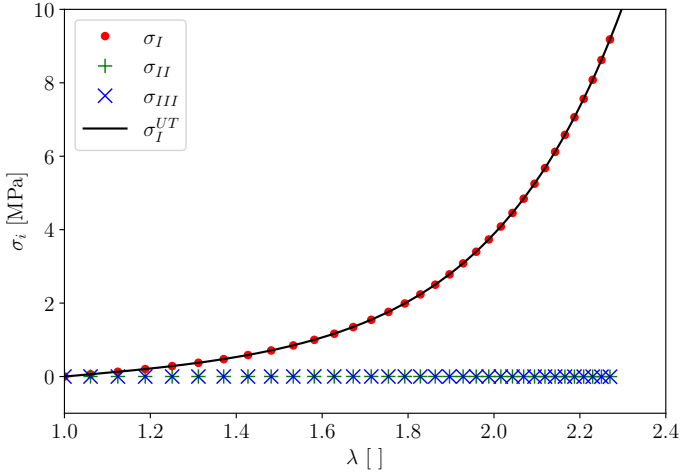

(b) Principal stresses σ_i as function of the largest principal stretch ratio λ_I.

Figure 13: uni-modal path $K_3 = 1$: comparison of numerical results with the analytical solution.

4.2. $K_3 = 0$: planar tension and simple shear

A similar method is employed to follow a loading path that maintain $K_3 = 0$ at the notch. In this case, a one-term interpolation is sufficient to accurately approximate the path, the corresponding function is

$$\tau(\lambda) = 0.324(\lambda - 1)^{0.377}. \tag{31}$$

The mode of deformation $K_3 = 0$ is associated to both planar tension (PT) (Yeoh, 2001) and simple shear (SS) (Nunes and Moreira, 2013). The Cauchy-Green strain tensors for planar tension, $\boldsymbol{b}^{PT}$, and simple shear, $\boldsymbol{b}^{PT}$, are the same in their corresponding principal bases ($\mathcal{B}_p^{PT}$ and $\mathcal{B}_p^{SS}$ respectively):

$$\boldsymbol{b}^{PT} = \boldsymbol{b}^{SS} = \begin{bmatrix} {\lambda_I}^2 & & \\ & {\lambda_{II}}^2 & \\ & & {\lambda_{III}}^2 \end{bmatrix} = \begin{bmatrix} {\lambda_I}^2 & & \\ & 1 & \\ & & 1/\lambda_I^2 \end{bmatrix}. \tag{32}$$

The kinematics of the planar tension is driven by the stretch ratio in the perpendicular direction of the clamps. The simple shear is described by the amount of shear γ and the largest principal stretch ratio λ_I is a function of γ:

$$\lambda_I^{SS} = \sqrt{\frac{\gamma^2 + 2 + \gamma\sqrt{\gamma^2 + 4}}{2}} \tag{33}$$

Nevertheless, the two corresponding true stress tensors, $\boldsymbol{\sigma}^{PT}$ and $\boldsymbol{\sigma}^{SS}$, differ. For planar tension, the plane stress assumption in the thickness di-

rection is adopted. Then

$$\boldsymbol{\sigma}^{PT} = \begin{bmatrix} \sigma_I^{PT} & & \\ & \sigma_{II}^{PT} & \\ & & 0 \end{bmatrix}_{\mathcal{B}_p^{PT}} \tag{34}$$

with

$$\sigma_I^{PT} = 2\frac{\partial W}{\partial I_1}\left({\lambda_I}^2 - \frac{1}{{\lambda_I}^2}\right) \approx 2\mu \sum_{i=1}^{5} i \frac{C_i}{{\lambda_m}^{2i-2}} {I_1}^{i-1}\left({\lambda_I}^2 - \frac{1}{{\lambda_I}^2}\right), \tag{35}$$

and

$$\sigma_{II}^{PT} = 2\frac{\partial W}{\partial I_1}\left(1 - \frac{1}{{\lambda_I}^2}\right) \approx 2\mu \sum_{i=1}^{5} i \frac{C_i}{{\lambda_m}^{2i-2}} {I_1}^{i-1}\left(1 - \frac{1}{{\lambda_I}^2}\right). \tag{36}$$

On the other hand, the simple shear test is carried out with blocks and it is difficult to identify the Lagrange multiplier associated with incompressibility, and then to isolate the stress tensor. Charlton and Yang showed that the largest principal stresses for simple shear and planar tension are linked by a universal relation (Charlton et al., 1994):

$$\frac{\sigma_I^{PT}}{\sigma_I^{SS}} = \frac{2\sqrt{\gamma^2+4}}{2+\gamma^2\left(1+\sqrt{1+\frac{4}{\gamma^2}}\right)} \tag{37}$$

In the present case, as the studied point is at the surface of the sample, the principal stress normal the the surface is null and the corresponding principal stretch ratio remains equal to one. Hence, the Cauchy stress tensor

is

$$\boldsymbol{\sigma} = \begin{bmatrix} \sigma_I^{SS} & & \\ & 0 & \\ & & \sigma_{III}^{SS} \end{bmatrix}_{\mathcal{B}_p^{SS}} \tag{38}$$

with

$$\sigma_I^{SS} = 2\frac{\partial W}{\partial I_1}\left({\lambda_I}^2 - 1\right), \tag{39}$$

and

$$\sigma_{III}^{SS} = 2\frac{\partial W}{\partial I_1}\left(\frac{1}{{\lambda_I}^2} - 1\right). \tag{40}$$

Figure 14 compares the eigenvalues obtained numerically with Abaqus and the analytical solution for both planar tension (Eqs. (35)-(36)) and simple shear (Eqs. (39)-(40)). As in the $K_3 = 1$ case, plots are drawn with respect of the reduced time for the largest principal stretch ratios (Fig. 14a) and with respect of the largest principal stretch ratio λ_I for the principal true stresses (Fig. 14b). It confirms the state of simple shear at the material point under consideration.

At present, we can only observe that the results correspond to simple shear in a specific case where one of the principal stresses is zero. In future work, we intend to investigate in more detail the still open question of the relation between simple shear and the planar tension and stress states. There is already a substantial literature on the subject (Belik and Fosdick, 1998, Destrade et al., 2012, Nunes and Moreira, 2013, Thiel et al., 2019).

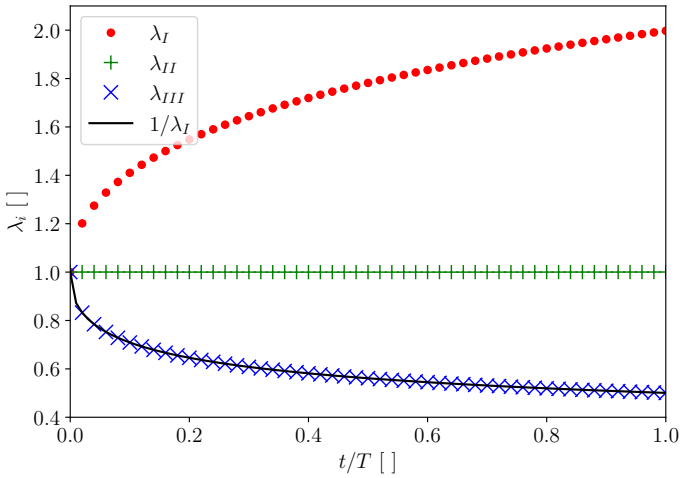

(a) Principal stretch ratios λ_i as function of reduced time t/T.

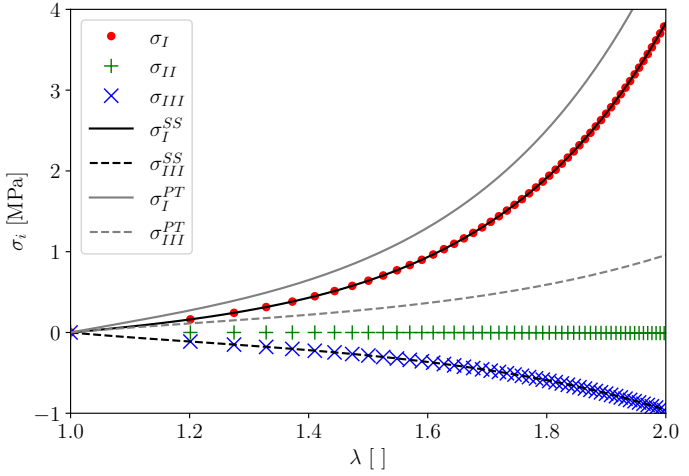

(b) Principal stresses σ_i as function of the largest principal stretch ratio λ_I.

Figure 14: uni-modal path $K_3 = 0$: comparison of numerical results with the analytical solution

5. Conclusion

In this work we offer a new perspective on the issue of multi-axiality in soft materials testing. Based on the logarithmic strain tensor, we propose to introduce the new concept of uni- and multi-modality. This term can be seen as the local counterpart of the widely used term multi-axiality, a term we reserve to a macroscopic point of view (related to the testing machine).

It as been shown the non-equivalence between axiality and modality. Thus to the numerical study of an AE2 specimen, we demonstrate that a uni-axial test is not a uni-modal test except in specific cases such as uni-axial tension.

We believe that the notion of modality has numerous and relevant applications. For example, it may be possible to produce a digital shadow of a complex part subjected to specific loads, evaluate the areas most at risk and use modality mapping to reproduce the same loads on a simple specimen to predict service life, a proposal for a multi-modal experimental campaign is given in the appendix. To close the paper, we now propose a detailed methodology and the necessary numerical tools for mapping the evolution of material intensity and mode for a given material point. These maps can then be used by an experimenter to build a multi-modal test campaign.

We believe that this work can be an important step towards better control of multiaxial tests, in particular tensile-torsion experiments, by providing a possible quantification of the strain and stress states induced by the loading conditions. Experimental loading conditions are currently chosen with no

justification other than to cover "a wide range of strain histories" (Mars and Fatemi, 2005) or "a wide range of fatigue lives" (Ayoub et al., 2012). By way of example, the present quantification avoids the pitfall encountered by Le Mire et al. (2021): for tensile-torsion tests, even large prescribed loading angles can produce almost uniaxial tensile tests along the gauge length.

CRediT authorship contribution statement

Benjamin Martin: Conceptualization, Methodology, Software, Formal analysis, Investigation, Data curation, Writing - Original draft, Visualization. **Erwan Verron**: Conceptualization, Validation, Investigation, Writing - Review & Editing, Supervision, Funding acquisition. **Michel Coret**: Conceptualization, Validation, Investigation, Writing - Review & Editing, Visualization, Supervision. **Nathan Selles**: Conceptualization, Validation, Investigation, Writing - Review & Editing, Supervision, Funding acquisition.

Declaration of competing interest

The authors declare that they have no known competing financial interests or personal relationships that could have appeared to influence the work reported in this paper.

Data availability

Data are accessible on Zenodo (Martin et al., 2024).

Acknowledgements

This study was funded by the French institution Association Nationale de la Recherche et de la Technologie (Grant number 2022/0668). For the purpose of open access, the author has applied a CC-BY public copyright licence to any Author Accepted Manuscript (AAM) version arising from this submission.

Appendix A. Detailed methodology

Here we propose an explicit methodology to build a multi-modal campaign of testing for a material. Such a campaign can be carried out with the following steps:

1. characterize the hyperelastic material to be studied, it will be required to implement a numerical model in a finite element software,
2. select a specimen geometry that localizes crack initiation and failure,
3. define the necessary deformation modes and intensities by choosing the values of K_2 and K_3 that are relevant for the studied case,
4. interpolate the input signals associated to the desired modes and intensities from the maps using the λ and τ quantities and convert it into U and α signal (it can also be done by directly interpolating U and α),
5. carry out the tests.

References

D. Ahmad and R. M. Ajaj. Multiaxial mechanical characterization of latex skin for morphing wing application. *Polymer Testing*, 106:107408, 2022. ISSN 0142-9418. doi: 10.1016/j.polymertesting.2021.107408.

E. M. Arruda and M. C. Boyce. A three-dimensional constitutive model for the large stretch behavior of rubber elastic materials. *Journal of the Mechanics and Physics of Solids*, 41(2):389 412, 1993. ISSN 0022-5096. doi: 10.1016/0022-5096(93)90013-6.

G. Ayoub, M. Naït-Abdelaziz, F. Zaïri, J.M. Gloaguen, and P. Charrier. A continuum damage model for the high-cycle fatigue life prediction of styrene-butadiene rubber under multiaxial loading. *International Journal of Solids and Structures*, 48(18):2458 2466, 2011. ISSN 0020-7683. doi: 10.1016/j.ijsolstr.2011.04.003.

G. Ayoub, M. N. Abdelaziz, F. Zaïri, J. M. Gloaguen, and P. Charrier. Fatigue life prediction of rubber-like materials under multiaxial loading using a continuum damage mechanics approach: Effects of two-blocks loading and R ratio. *Mechanics of Materials*, 52:87 102, 2012. ISSN 0167-6636. doi: 10.1016/j.mechmat.2012.03.012.

M. Baker and J. L. Ericksen. Inequalities restricting the form of the stress-deformation relations for isotropic elastic solids and Reiner-Rivlin fluids.

Journal of the Washington Academy of Sciences, 44(2):33 35, 1954. ISSN 00430439.

P. Belik and R. Fosdick. The state of pure shear. *Journal of Elasticity*, 52: 91 98, 1998. doi: 10.1023/A:1007500316569.

S. Belkhiria, A. Hamdi, and R. Fathallah. Strain-based criterion for uniaxial fatigue life prediction for an SBR rubber: Comparative study and development. *Proceedings of the Institution of Mechanical Engineers, Part L: Journal of Materials: Design and Applications*, 234(7):897 909, 2020. doi: 10.1177/1464420720913595.

Y. Bitoh, N. Akuzawa, K. Urayama, T. Takigawa, M. Kidowaki, and K. Ito. Peculiar nonlinear elasticity of polyrotaxane gels with movable cross-links revealed by multiaxial stretching. *Macromolecules*, 44(21):8661 8667, 2011. doi: 10.1021/ma201530z.

M. C. Boyce and E. M. Arruda. Constitutive models of rubber elasticity: A review. *Rubber Chemistry and Technology*, 73(3):504 523, 2000. ISSN 0035-9475. doi: 10.5254/1.3547602.

R. M. Brannon. *Elements of Phenomenological Plasticity: Geometrical Insight, Computational Algorithms, and Topics in Shock Physics*, volume 2, pages 225 274. 2007. ISBN 978-3-540-22364-1. doi: 10.1007/978-3-540-68408-4_6.

J. C. Case, E. L. White, and R. K. Kramer. Soft material characterization for robotic applications. *Soft Robotics*, 2(2):80 87, 2015. doi: 10.1089/soro.2015.0002.

D. J. Charlton, J. Yang, and K. K. Teh. A review of methods to characterize rubber elastic behavior for use in finite element analysis. *Rubber chemistry and technology*, 67(3):481 503, 1994.

P. Ciarletta and M. Destrade. Torsion instability of soft solid cylinders. *IMA Journal of Applied Mathematics*, 79(5):804 819, 2014. doi: 10.1093/imamat/hxt052.

J. C. Criscione, J. D. Humphrey, A. S. Douglas, and W. C. Hunter. An invariant basis for natural strain which yields orthogonal stress response terms in isotropic hyperelasticity. *Journal of the Mechanics and Physics of Solids*, 48(12):2445 2465, 2000. ISSN 0022-5096. doi: 10.1016/S0022-5096(00)00023-5.

M. Destrade, J. G. Murphy, and G. Saccomandi. Simple shear is not so simple. *International Journal of Non-Linear Mechanics*, 47(2):210 214, 2012. ISSN 00207462. doi: 10.1016/j.ijnonlinmec.2011.05.008.

M. Flamm, J. Spreckels, T. Steinweger, and U. Weltin. Effects of very high loads on fatigue life of NR elastomer materials. *International Journal of Fatigue*, 33(9):1189 1198, 2011. ISSN 0142-1123. doi: 10.1016/j.ijfatigue.2011.03.008.

S. Gour and D. Kumar. Constitutive modeling of particle reinforced rubber-like materials. *Theoretical and Applied Mechanics Letters*, 12(6):100383, 2022. ISSN 2095-0349. doi: 10.1016/j.taml.2022.100383. URL https://doi.org/10.1016/j.taml.2022.100383.

S.V. Hainsworth. An environmental scanning electron microscopy investigation of fatigue crack initiation and propagation in elastomers. *Polymer Testing*, 26(1):60 70, 2007. ISSN 0142-9418. doi: 10.1016/j.polymertesting.2006.08.007.

R. J. Harbour, A. Fatemi, and W. V. Mars. Fatigue life analysis and predictions for NR and SBR under variable amplitude and multiaxial loading conditions. *International Journal of Fatigue*, 30(7):1231 1247, 2008. ISSN 0142-1123. doi: 10.1016/j.ijfatigue.2007.08.015.

G. A. Holzapfel. *Nonlinear solid mechanics: a continuum approach for engineering science*. Kluwer Academic Publishers Dordrecht, 2002. ISBN 978-0-0471-82319-3.

S. Kawabata, M. Matsuda, K. Tei, and H. Kawai. Experimental survey of the strain energy density function of isoprene rubber vulcanizate. *Macromolecules*, 14(1):154 162, 1981. doi: 10.1021/ma50002a032. URL https://doi.org/10.1021/ma50002a032.

J. Kim, S. Lee, C.Y Gu, T.S Kim, H. Kong, and D. Jang. Mechanical characterization of collagen hydrogels by quasistatic uniaxial tensile ex-

periments. *Advanced Engineering Materials*, 25(21):2301136, 2023. doi: 10.1002/adem.202301136.

B. A. Lane, K. A. Harmon, R. L. Goodwin, M. J. Yost, T. Shazly, and J. F. Eberth. Constitutive modeling of compressible type-I collagen hydrogels. *Medical Engineering & Physics*, 53:39 48, 2018. ISSN 1350-4533. doi: 10.1016/j.medengphy.2018.01.003.

J.-B. Le Cam, B. Huneau, and E. Verron. Fatigue damage in carbon black filled natural rubber under uni- and multiaxial loading conditions. *International Journal of Fatigue*, 52:82 94, 2013. ISSN 0142-1123. doi: 10.1016/j.ijfatigue.2013.02.022. URL `https://doi.org/10.1016/j.ijfatigue.2013.02.022`.

E. Le Mire. *Contributions expérimentales et théoriques à la fatigue multiaxiale des élastomères : Vers un critère cinématique*. Theses, École centrale de Nantes, 2022.

E. Le Mire, E. Verron, B. Huneau, and N. Selles. Multiaxial fatigue experiments for elastomers based on true strain invariants. *Journal of Rubber Research*, 24(2):227 236, 2021. ISSN 2524-3993. doi: https://doi.org/10.1007/s42464-021-00088-6.

A. S. Lectez, E. Verron, and B. Huneau. How to identify a hyperelastic constitutive equation for rubber-like materials with multiaxial tensiontorsion

experiments. *International Journal of Non-Linear Mechanics*, 65:260 270, 2014. ISSN 0020-7462. doi: 10.1016/j.ijnonlinmec.2014.06.007.

R. Luo. Effective stress criterion for rubber multiaxial fatigue under both proportional and non-proportional loadings. *Engineering Failure Analysis*, 121:105172, 2020. doi: 10.1016/j.engfailanal.2020.105172.

G. Marckmann and E. Verron. Comparison of hyperelastic models for rubber-like materials. *Rubber Chemistry and Technology*, 79:835 858, 2006. doi: 10.5254/1.3547969.

W. V. Mars and A. Fatemi. Multiaxial fatigue of rubber: Part ii: experimental observations and life predictions. *Fatigue & Fracture of Engineering Materials & Structures*, 28(6):523 538, 2005. doi: 10.1111/j.1460-2695.2005.00895.x. URL `https://doi.org/10.1111/j.1460-2695.2005.00895.x`.

B. Martin, M. Coret, N. Selles, and E. Verron. Mapping of the invariants K_2 and K_2 of the Hencky's tensor., 2024. URL `https://doi.org/10.5281/zenodo.10697022`.

L.C.S. Nunes. Shear modulus estimation of the polymer polydimethylsiloxane (pdms) using digital image correlation. *Materials & Design*, 31(1):583 588, 2010. ISSN 0261-3069. doi: 10.1016/j.matdes.2009.07.012. URL `https://doi.org/10.1016/j.matdes.2009.07.012`.

L.C.S. Nunes and D.C. Moreira. Simple shear under large deformation: Experimental and theoretical analyses. *European Journal of Mechanics - A/Solids*, 42:315 322, 2013. ISSN 09977538. doi: 10.1016/j.euromechsol.2013.07.002.

R. S. Rivlin and E. K. Rideal. Large elastic deformations of isotropic materials vi. further results in the theory of torsion, shear and flexure. *Philosophical Transactions of the Royal Society of London. Series A, Mathematical and Physical Sciences*, 242(845):173 195, 1949. doi: 10.1098/rsta.1949.0009.

N. Saintier, G. Cailletaud, and R. Piques. Crack initiation and propagation under multiaxial fatigue in a natural rubber. *International Journal of Fatigue*, 28(1):61 72, 2006a. ISSN 0142-1123. doi: 10.1016/j.ijfatigue.2005.03.006.

N. Saintier, G. Cailletaud, and R. Piques. Multiaxial fatigue life prediction for a natural rubber. *International Journal of Fatigue*, 28(5):530 539, 2006b. ISSN 0142-1123. doi: 10.1016/j.ijfatigue.2005.05.011. URL `https://doi.org/10.1016/j.ijfatigue.2005.05.011`. Selected papers from the 7th International Conference on Biaxial/Multiaxial Fatigue and Fracture (ICBMFF).

Scipy Community. docs.scipy.org/doc/scipy/ reference/generated/scipy.interpolate.rbf.html. Visited on 2023-11-14.

W. B. Shangguan, X. L. Wang, J. X. Deng, S. Rakheja, X. Y. Pan, and B. Yu. Experiment and modeling of uniaxial tension fatigue performances for filled natural rubbers. *Materials & Design*, 58:65 73, 2014. ISSN 0261-3069. doi: 10.1016/j.matdes.2014.01.035.

N. Suphadon and J. J. C. Busfield. Elastic behaviour of rubber cylinders under combined torsion and tension loading. *Plastics, Rubber and Composites*, 38(8):337 342, 2009. doi: 10.1179/146580109X12473409436788.

Y. L. Tee, M. S. Loo, and A. Andriyana. Recent advances on fatigue of rubber after the literature survey by Mars and Fatemi in 2002 and 2004. *International Journal of Fatigue*, 110:115 129, 2018. ISSN 0142-1123. doi: 10.1016/j.ijfatigue.2018.01.007.

C. Thiel, J. Voss, R. J. Martin, and P. Neff. Shear, pure and simple. *International Journal of Non-Linear Mechanics*, 112:57 72, 2019. ISSN 0020-7462. doi: 10.1016/j.ijnonlinmec.2018.10.002.

L. R. G. Treloar. Stress-strain data for vulcanised rubber under various types of deformation. *Transaction of the Faraday Society*, 40:59 70, 1944. doi: 10.1039/TF9444000059.

S. Wang and S. A. Chester. Experimental characterization and continuum modeling of inelasticity in filled rubber-like materials. *International Journal of Solids and Structures*, 136-137:125 136, 2018. ISSN 0020-7683. doi: 10.1016/j.ijsolstr.2017.12.010.

D.G. Yang, K.M.B. Jansen, L.J. Ernst, G.Q. Zhang, H.J.L. Bressers, and J.H.J. Janssen. Effect of filler concentration of rubbery shear and bulk modulus of molding compounds. *Microelectronics Reliability*, 47(2):233 239, 2007. ISSN 0026-2714. doi: 10.1016/j.microrel.2006.09.031. URL https://doi.org/10.1016/j.microrel.2006.09.031.

O. H. Yeoh. Analysis of deformation and fracture of pure shear rubber testpiece. *Plastics, Rubber and Composites*, 30(8):389 397, 2001. doi: 10.1179/146580101101541787.

Highlights

Towards a rational approach for multi-axial experimental campaigns for rubberlike material

Benjamin Martin, Erwan Verron, Michel Coret, Nathan Selles

- Contribution to experimental techniques for characterizing rubberlike materials.
- Emphasis on local rather than global multi-axial strain and stress states.
- Proposal to revisit multi-axiality definition from a material viewpoint.
- Introduction of the concept of "modality" to describe local modes of deformation.
- Methodology for developing multi-modal experimental campaigns for elastomers.